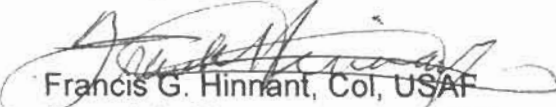




MEMORANDUM FOR: SAF/PAS  
1690 Air Force Pentagon - 5D227  
Washington DC 20330-1690

JUN 10 2002

FROM:

  
Francis G. Hinnant, Col, USAF  
Associate Director of Acquisition  
NPOESS Integrated Program Office  
8455 Colesville Rd, Suite 1450  
Silver Spring, MD 20910

SUBJECT: Paper approval for: Proton Irradiations of Large Area  $\text{Hg}_{1-x}\text{Cd}_x\text{Te}$   
Photovoltaic Detectors for the Cross-track Infrared Sounder

Enclosed are the required ten (10) copies of the subject paper. This paper will be released at the annual meeting of SPIE (International Society for Optical Engineering) in July of '02. It was written by employees of MIT Lincoln Laboratory, DRS Sensors & Targeting Systems, ITT Aerospace/Communications Division, and Harvard Cyclotron Lab. It will be presented by employees of ITT Industries.

The program office has reviewed the information in the attached papers and found it appropriate for public disclosure without change.

Point of contact on this matter is Capt. Christina Muth, NPOESS IPO/ADA at 301-427-2084 (Ext. 114).

Attachment: Presentation—10 copies

# Proton Irradiations of Large Area $\text{Hg}_{1-x}\text{Cd}_x\text{Te}$ Photovoltaic Detectors for the Cross-track Infrared Sounder

M.W. Kelly<sup>a</sup>, E.J. Ringdahl<sup>a</sup>, A.I. D'Souza<sup>b</sup>, S.D. Luce<sup>c</sup>, and E.W. Cascio<sup>d</sup>

<sup>a</sup> MIT Lincoln Laboratory, 244 Wood St., Lexington, MA 02420

<sup>b</sup> DRS Sensors & Targeting Systems, 3400 Miraloma Ave., Anaheim, CA 92806

<sup>c</sup> ITT Aerospace/Communications Division, Ft. Wayne, IN 46801

<sup>d</sup> Harvard Cyclotron Lab, 44 Oxford St., Cambridge, MA 02138

## ABSTRACT

The effect of radiation on  $\text{Hg}_{1-x}\text{Cd}_x\text{Te}$  photodiodes is an important parameter to understand when determining the long-term performance limitations for the Cross-track Infrared Sounder (CrIS), a Fourier Transform interferometric sensor that will fly as part of the National Polar-orbiting Operational Environmental Satellite System (NPOESS). The CrIS sensor uses relatively large area photovoltaic detectors, 1 mm in diameter. Each p-on-n  $\text{Hg}_{1-x}\text{Cd}_x\text{Te}$  photodiode consists of MBE grown, n-type material on lattice matched CdZnTe, with arsenic implantation used to form the junction. A 1mm diameter detector is achieved by using a lateral collection architecture. Solar, and trapped protons are a significant source of radiation in the NPOESS 833 km orbits. We irradiated 22 LWIR detectors with protons at the Harvard Cyclotron Laboratory (HCL) and monitored the I-V performance and dynamic impedance of each detector. Three groups of detectors were irradiated with either 44, 99, or 153-MeV protons, each between  $1 \times 10^{10}$  -  $4 \times 10^{12}$  p<sup>+</sup>/cm<sup>2</sup> (total range ~ 0.7 - 690 krad(Si)). Several I-V data sets were collected within that fluence range at all three energies. All the detectors were warmed to room temperature for approximately 96 hours following the largest proton dose, re-cooled, and then re-characterized in terms of I-V performance and dynamic impedance. The total noise increase predicted for CrIS after 7-years in orbit is less than 1%.

**Keywords:**  $\text{Hg}_{1-x}\text{Cd}_x\text{Te}$  detectors, radiation tolerance, fourier transform spectrometer, remote sensing

## 1.0 BACKGROUND

A new era of operational polar-orbiting environmental satellites will be launched for the first time around 2008. NPOESS is a tri-agency venture between NOAA, NASA, and DoD, which merges civilian (POES) and defense (DMSP) polar meteorological satellite programs onto a single platform. The NPOESS satellites will eventually replace both two-satellite constellations. The NPOESS constellation will operate in an 833 km, 98.7° inclination, near sun-synchronous orbit. Currently three orbital planes are planned with 1330, 1730, and 2130 local equatorial ascending crossing times. In 1999, ITT Industries in Ft. Wayne, IN was awarded the contract to build CrIS. Meeting demanding noise performance requirements requires careful sensor design to achieve a detection-limited system.<sup>1,2</sup> In this work we quantify the effects caused by exposure of the CrIS long-wave infrared (LWIR) photodetectors to energetic protons; which is one mechanism that could affect system performance over the life of the instrument.

### 1.1. CrIS Detection Limited Noise Performance

The CrIS detectors are p-on-n double layer planar heterostructure (DLPH) diodes<sup>3</sup>. The DLPH architecture<sup>4</sup> reduces surface generation-recombination and tunneling currents by incorporating a buried narrow-bandgap active layer in the DLPH architecture. MBE is used to grow n-type  $\text{Hg}_{1-x}\text{Cd}_x\text{Te}$  on lattice matched CdZnTe. The wafer material is grown with wider bandgap cap layers. The required 1000  $\mu\text{m}$  diameter detectors were manufactured using the lateral collection diode (LCD) architecture<sup>5</sup> to reduce the probability of a

performance degrading defects<sup>6</sup> intersecting the p/n junction. The 1000  $\mu\text{m}$  diameter detector consists of 2298 p-type implants tied together at the metal level to form a single large detector. The detector geometry is back-illuminated; i.e. photons traverse the transparent CdZnTe and impinge on the absorbing n-type material, opposite the p/n junction. Absorbed photons create electron-hole pairs. Minority carriers generated within a diffusion length of the junction contribute to current flow. Figure 1 shows the LCD detector and back-illuminated DLPH architecture.

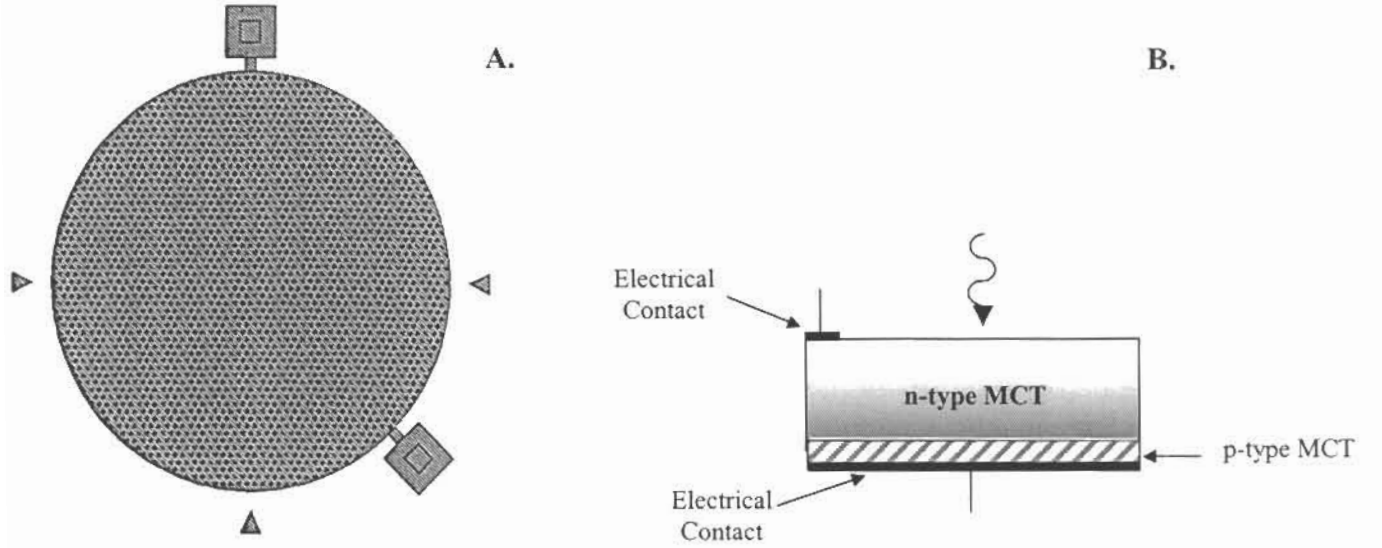


**Figure 1.** A. 1 mm CrIS diodes consisting of 2298 small implants, tied together in a metal layer. B. Back-illuminated p on n photovoltaic detector

The detection-limited performance of the CrIS sensor can be examined by considering the mechanisms for noise within the detection circuit. The noise equivalent spectral radiance (NESR) is directly proportional to the total noise current,  $I(f)_T$ . The diodes are operated relatively warm;  $T = 81\text{K}$  (LW) and  $T = 98\text{K}$  (MW & SW), and reverse biased at  $V_b \approx -60\text{mV}$ . The bias is optimized to present the highest possible source impedance to the preamplifier. A resistive transimpedance preamplifier provides enough gain to render the noise in down-stream electronics negligible. The dominant noise mechanisms are: dark current ( $I_d$  Amps) shot noise, photocurrent ( $I_{s\_ph} + I_{b\_ph}$  Amps) shot noise,  $1/f$  noise in the diode, and amplifier noise. The total noise current in terms of  $\text{A}/\text{Hz}^{1/2}$  can be written:

$$I(f)_T = \sqrt{2qI_d + 2q(I_{s\_ph} + I_{b\_ph}) + \frac{\alpha^2 I_d^2}{f} + \left(\frac{V_{pa}}{R_d}\right)^2} \quad (1.1)$$

Where  $q$  is the electronic charge unit,  $1.6 \times 10^{-19}$  Coulombs. Since CrIS is an AC coupled FTS, and time domain signal data is transformed into the frequency domain to recover the earth's radiant spectrum, the spectral content of the noise is an important consideration, particularly in the long-wave region of the spectrum. The  $1/f$  noise contribution is modeled according to [7]. The  $1/f$  noise is proportional to the dark current multiplied by a dimensionless quantity,  $\alpha$ , measured to be on the order of  $1\text{-}2 \times 10^{-5}$  for the CrIS LWIR detectors.<sup>8</sup> The preamplifier contribution to the total noise depends on the voltage noise of the input stage ( $V_{pa}$   $\text{V}/\text{Hz}^{1/2}$ ) and dynamic impedance of the detector ( $R_d$   $\Omega$ ). It is determined by measuring  $-dV/dI$ . The input referred preamplifier noise current and  $1/f$  noise voltage in the CrIS signal band are expected to

be negligible, and were not included in equation 1. The dark current component in equation 1 is expected to have several components

$$I_d = I_o e^{\frac{-qV_b}{kT}} + I_o + I_T + I_{DEF} \quad (1.2)$$

Where  $I_{DEF}$  are lattice defect related current mechanisms, and  $I_T$  is band-to-band tunneling current. Defect related current mechanisms include Shockley-Read diffusion, surface generation-recombination, depletion region generation-recombination, and trap-assisted tunneling.<sup>9,10</sup> At the beginning of life the CrIS detectors can achieve near thermal diffusion limited dark current. The present study seeks to quantify how defects caused by protons interacting with the detector material increase the dark current, and how the noise performance of the CrIS may be affected. Although not characterized in this study, the quantum efficiency could also be affected by the proton irradiation. This issue will be discussed in section 4 of this paper.

## 1.2 CrIS Radiation Environment

The radiation environment for the CrIS has been defined in the NPOEES General Instrument Interface Document<sup>11</sup> (GIID). The sensor must be capable of meeting all performance parameters over a seven-year mission when exposed to the trapped proton, solar flare proton, and trapped electron spectra shown in figure 2. Additionally a factor of two design margin is mandated. The total dose requirement for

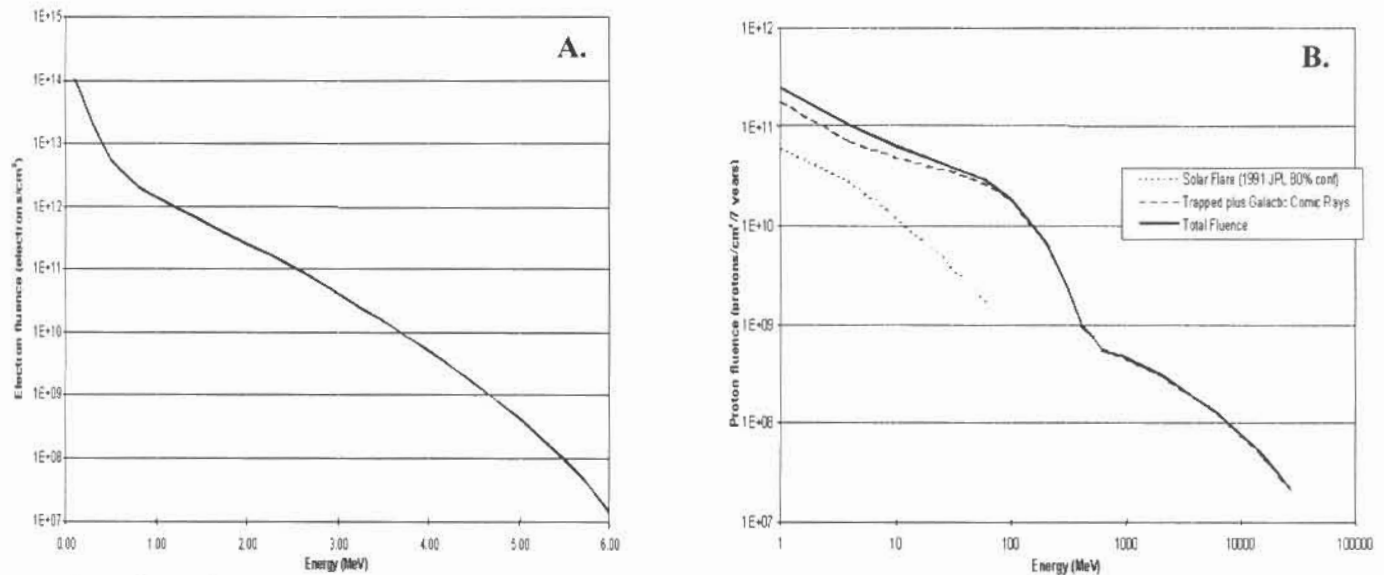


Figure 2. A. Electron and B. Proton environment as specified in the GIID

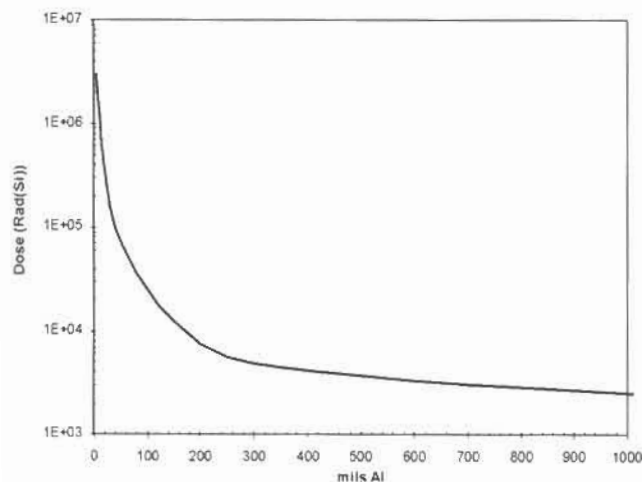


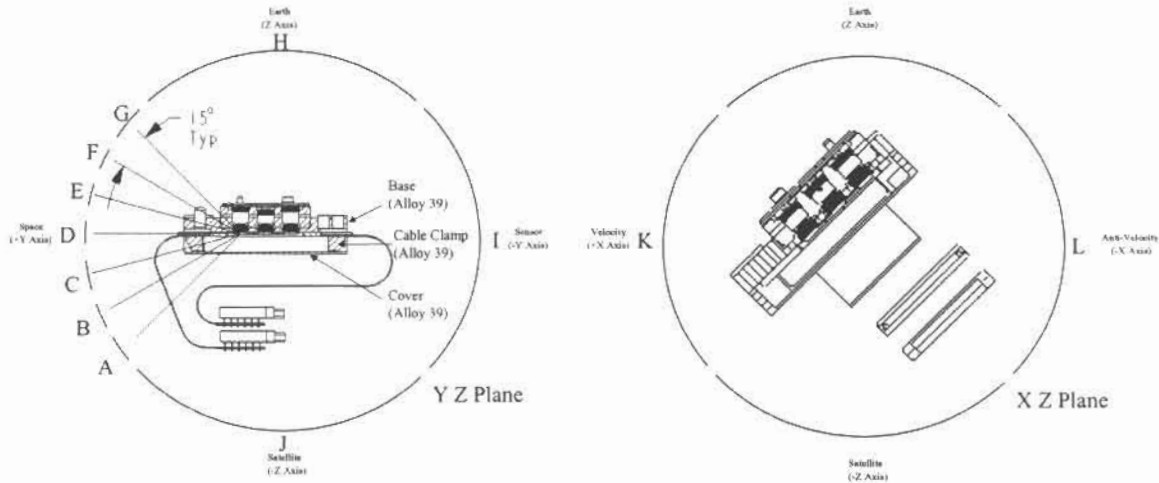
Figure 3. Total dose environment as specified in the GIID

Table 1. Total dose environment as specified in the GIID broken into source components

Shielding Mils (AL)	Trapped Protons Rad(Si)/7 Yr	Trapped Electrons Rad(Si)/7 Yr	Solar Flare Protons Rad(Si)/7 Yr	Total Rad(Si)/7 Yr
100	6.50 E03	1.81 E04	1.56 E03	2.62 E04
200	4.79 E03	2.06 E03	7.12 E02	7.56 E03
400	3.67 E03	6.76 E01	4.06 E02	4.14 E03
600	3.05 E03	4.35 E01	0.00 E00	3.09 E03
1000	2.25 E03	3.04 E01	0.00 E00	2.28 E03

internal electrical components is plotted in figure 3 as a function of equivalent shielding thickness. The contribution from protons and electrons is delineated for several shield thickness values in table 1.

The CrIS detectors are positioned within the FPA module and mounted to a passive radiator, which has a clear view to space. The FPA module was analyzed in two planes (Y-Z and X-Z) for a first order estimate of the equivalent aluminum shielding thickness provided by the sensor. Each plane was then divided into four 90-degree. The quadrant that is most susceptible to radiation is the space-viewing quadrant identified in the Y-Z Plane. This 90-degree quadrant was then broken down into six 15-degree



**Figure 4.** CrIS detector assembly and the geometrical coordinates identified for radiation shielding analysis

increments, identified "A" thru "G" to estimate the total radiation shielding that exists in this quadrant. Figure 4 shows the detector assembly and the geometrical coordinates identified for analysis. The materials and respective densities that are present within the module design are listed in table 2.

**Table 2.** Relevant materials used in the CrIS sensor

Material	Density g/cm <sup>3</sup>	Density Ratio Material/Al
6061-T6 Aluminum	2.71	1
AlBeMet AM162	2.10	0.77
Beryllium SF200	1.85	0.68
Alloy 39	8.11	2.99
G10	1.80	0.66
Ceramic	2.49	0.92

The ratio of the material density to that of aluminum is also included. The effective aluminum shielding was determined by adding-up the thickness of each material within each quadrant angular field of view, extending from the outside of the sensor to the nearest detector, and multiplying by the density ratio. The analysis does not take into account manufacturing tolerances, the passive cooler honeycomb structure, MLI thermal blankets, or part plating. Table 3 summarizes each material thickness in each quadrant and the equivalent aluminum thickness. The minimum aluminum equivalent shielding thickness was 80-mils. The most sensitive Y-Z quadrant conservatively provides 500-mils shielding. The equivalent shielding averaged over the entire  $4\pi$  steradian sphere surrounding the detectors is even greater, however without much more proton stopping power according to figure 3. As a conservative estimate for this analysis, 8 krad(Si) radiation dose will be assumed for end-of-life performance estimates. This includes the required 2x GIID margin factor.

**Table 3.** Spreadsheet for effective aluminum shielding calculation

Quadrant	Part	Base Material	Thickness (in)	Ratio Factor	Effective Aluminum (in)
<b>A</b>	Emitter (Stage 4)	Be	0.043	0.68	0.029
	FPA Rear Cover	Alloy 39	0.017	2.99	0.051
					0.08
<b>B</b>	Emitter (Stage 4)	Be	0.043	0.68	0.029
	FPA Rear Cover	Alloy 39	0.017	2.99	0.051
					0.08
<b>C</b>	Emitter (Stage 4)	Be	0.043	0.68	0.029
	Cable Clamp	Alloy 39	0.156	2.99	0.466
					0.496
<b>D</b>	Emitter (Stage 4)	Be	0.043	0.68	0.029
	Flex Stiffener	G10	0.335	0.66	0.221
	CMLB	Ceramic	0.26	0.92	0.239
					0.49
<b>E</b>	Emitter (Stage 4)	Be	0.25	0.68	0.17
	FPA Base	Alloy 39	0.5	2.99	1.495
					1.665
<b>F</b>	Emitter (Stage 4)	Be	0.375	0.68	0.255
	Emitter (Stage 3)	Be	0.625	0.68	0.425
	Housing (Stage 3)	Al	0.375	1	0.375
	Housing (Stage 4)	Al	0.625	1	0.625
	FPA Base	Alloy 39	0.375	2.99	1.121
					2.801
<b>G</b>	Exceeds 1 inch of Aluminum equivalent material shielding thickness				
<b>H</b>	Exceeds 1 inch of Aluminum equivalent material shielding thickness				
<b>I</b>	Exceeds 1 inch of Aluminum equivalent material shielding thickness				
<b>J</b>	Exceeds 1 inch of Aluminum equivalent material shielding thickness				
<b>K</b>	Thermal Shield	Al	0.02	1	0.02
	Vac Hsg Cover	Al	0.032	1	0.032
	Vac Hsg (Stage 1)	AlBeMet	0.078	0.77	0.06
	Flexure Shield (Stage 2)	Al	0.02	1	0.02
	Flexure Bracket (Stage 2)	AlBeMet	0.06	0.77	0.046
	Radiator (Stage 2)	AlBeMet	0.156	0.77	0.12
	Shield (Stage 3)	Al	0.02	1	0.02
	Housing (Stage 3)	Al	0.125	1	0.125
	FPA Rear Cover	Alloy 39	0.017	2.99	0.051
					0.494
	Thermal Shield	Al	0.02	1	0.02
	Vac Hsg Cover	Al	0.032	1	0.032
<b>L</b>	Vac Hsg (Stage 1)	AlBeMet	0.078	0.77	0.06
	Vac Hsg (Stage 1)	AlBeMet	0.156	0.77	0.12
	Flexure Shield (Stage 2)	Al	0.02	1	0.02
	Flexure Bracket (Stage 2)	AlBeMet	0.06	0.77	0.046
	Radiator (Stage 2)	AlBeMet	0.078	0.77	0.06
	Shield (Stage 3)	Al	0.02	1	0.02
	Housing (Stage 3)	Al	0.06	1	0.06
	Housing (Stage 4)	Al	0.05	1	0.05
	Housing (Stage 4)	Al	0.06	1	0.06
	FPA Rear Cover	Alloy 39	0.017	2.99	0.051
					0.599

## 2.0 EXPERIMENTAL PROCEDURE

Risk reduction activities for CrIS involved fabricating detectors in all three channels for engineering unit (EU) demonstrations. The EUs focused on demonstrating all technical specifications needed to meet performance requirements. The LWIR detectors were the most challenging devices to fabricate, and as such produced more spares than the MWIR or SWIR EUs, i.e. rejected detectors that met nearly all performance requirements. There were twenty-two LWIR detectors available for destructive radiation testing. The devices were mounted into standard 64-pin leadless chip carriers (LLCC). The twenty-two detectors were divided into three groups with eight, eight, or six viable detectors mounted in

each LLCC. The LLCCs were mounted into a socket mechanically constrained with a G10 curb and clamped into place with a 100-mil aluminum cover. Figure 5 shows the assembly.

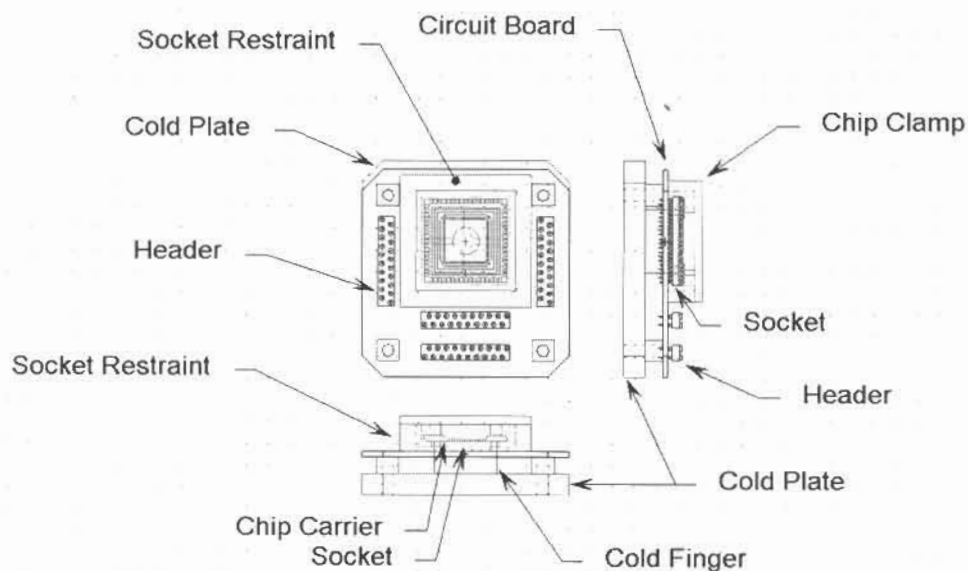


**Figure 5.** 64-pin LLCC socket assembly and cold finger for mounting the detectors into the LN2 dewar.

The circuit board was mounted through standoffs onto a copper-plate/cold-finger assembly which was clamped directly to the cold base of a liquid nitrogen dewar. The cover was sufficiently cold for dark I-V

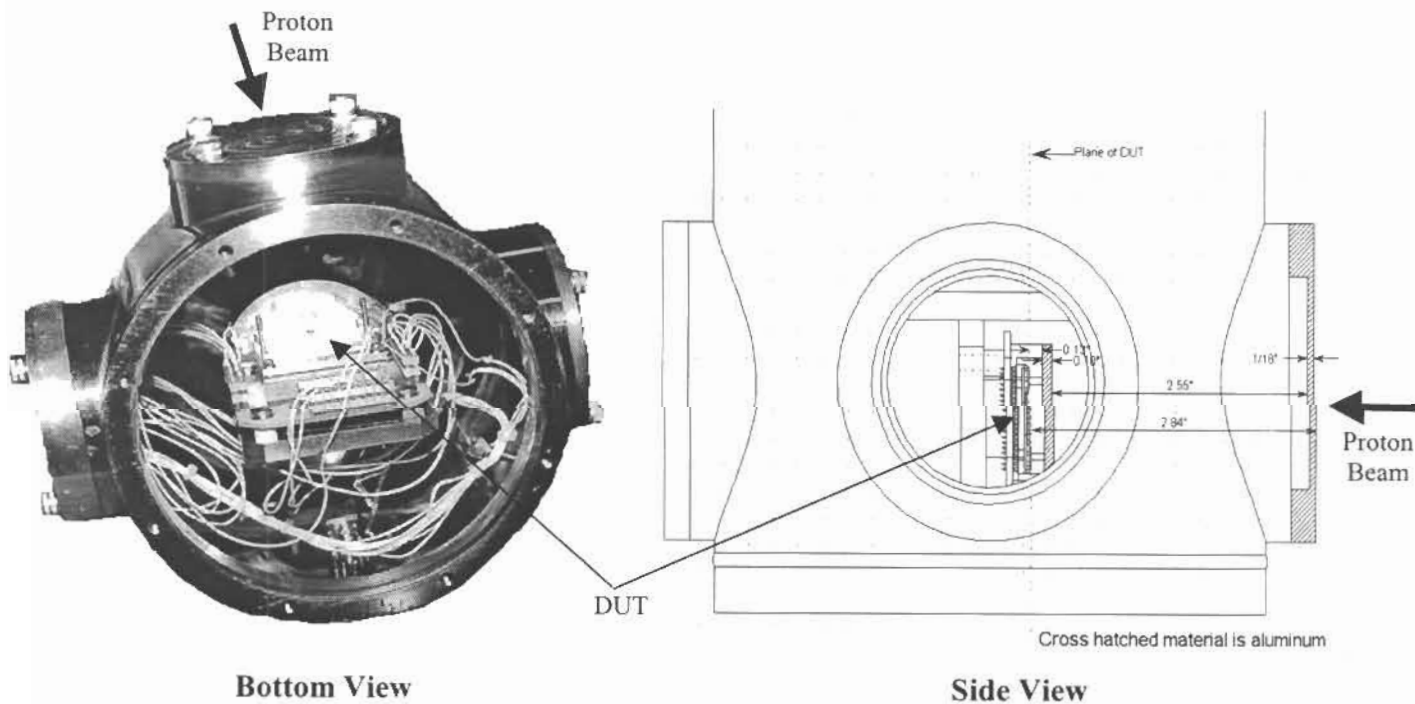


**Figure 6.** LN2 dewar assembly with cold mechanical assembly showing geometry and shielding used for proton irradiation



measurements. A platinum resistor was epoxied directly onto the cold finger to monitor temperature of the device under test (DUT). The dewar was evacuated and the DUT was maintained at approximately 78K for all proton irradiations and I-V measurements. A 62.5-mil aluminum cover was used to close the dewar port normal to the proton beam.

The facility used for irradiations was the Harvard Cyclotron Lab, in Cambridge Massachusetts. The accelerator is a synchrocyclotron that produces a fixed energy proton beam of 158.5-MeV. Introducing energy degraders into the beamline produces lower energy beams. The degraders also scatter the focused beam to uniformly cover any necessary field size. The degraders were composed of an acrylic resin, lead, or a combination of both materials, depending on the amount of absorption and/or scattering needed. The fluence was monitored during irradiations with a transmission (thin foil) ion chamber installed in the beam collimator, downstream of the degraders. Before the irradiation the signal produced in this ion chamber was calibrated to a faraday cup placed at the position of the target. Each of the three DUTs was exposed to only a single fixed proton energy beam: 44, 99, or 153-MeV between  $10^{10} - 4 \times 10^{12} \text{ p}^+/\text{cm}^2$ . The proton energy and fluence was initially calibrated external to the dewar. The beam parameters were then calculated at the DUT using the geometry and position of the aluminum dewar cover and LLCC cold clamp preceding the DUT in the beamline. Emulsion films were used in place of the DUT to verify the beam profile.

A laptop computer with a National Instruments PCMCIA 12-bit, 16-channel data acquisition (DAQ) card was used to collect data from up to nine detectors simultaneously. The DAQ analog voltage output was appropriately attenuated to sweep the bias on each diode in the DUT from -200 to +100 mV. A resistive transimpedance amplifier for each of nine channels converted the diode dark current to a voltage read by the DAQ.

### 3.0 RESULTS

An I-V data set was recorded just prior to each proton irradiation. The temperature was monitored during each measurement and remained stable to less than 0.2K. Table 4 shows the equivalent rad(Si) conversion used for the requirements analysis, and the 8-krad(Si) GIID requirement for the CrIS detectors.<sup>12</sup>

**Table 4.** Proton fluence to rad(Si) conversion and GIID requirement

Energy (MeV)	Conv. (rad(Si)/ ( $\text{p}^+/\text{cm}^2$ ))	8 krad(Si)Fluence Req ( $\text{p}^+/\text{cm}^2$ )
44	$1.7 \times 10^{-7}$	$4.7 \times 10^{10}$
99	$9.3 \times 10^{-8}$	$8.5 \times 10^{10}$
153	$6.9 \times 10^{-8}$	$1.2 \times 10^{11}$

Figure 7 shows a typical set of fourteen I-V curves for three diodes, one at each proton energy. The curves correspond to before the irradiation, after exposure to protons at various fluence intervals, and following approximately 96-hours of room temperature storage. In general, the change in dark current is small following lower fluence exposures, and increases as  $4 \times 10^{12} \text{ p}^+/\text{cm}^2$  is approached. The dynamic impedance at -60 mV bias decreased with increasing fluence, for all proton energy exposures. The I-V and dynamic impedance behavior following the room temperature annealing period varied depending on the group of diodes, and apparently proton energy the group was exposed, see figure 7. Quantitative details of each energy trial are presented below.

Figures 8 and 9 show the change in dark current and dynamic impedance respectively, at -10, -60, -100, and -180 mV reverse bias. Each data point is the mean of all detectors irradiated following each proton exposure at the specified proton energy. Absent data points in figure 8 A, B and C, for 44 and 99-MeV, at lower reverse bias, indicates zero or very slight decrease in the magnitude of dark current (on the order of  $10^{-7}$  Amps max). The data points corresponding to 8-krad(Si) are circled at the -60 mV CrIS bias point. At those points, dark current increased by approximately  $2 \times 10^{-7} - 2 \times 10^{-6}$  Amps, depending on proton energy. The higher energy protons induced more dark current than the lower. The dynamic impedance increase was between approximately 0 - 200  $\Omega$ . Again, the detectors were more sensitive to high-energy protons.



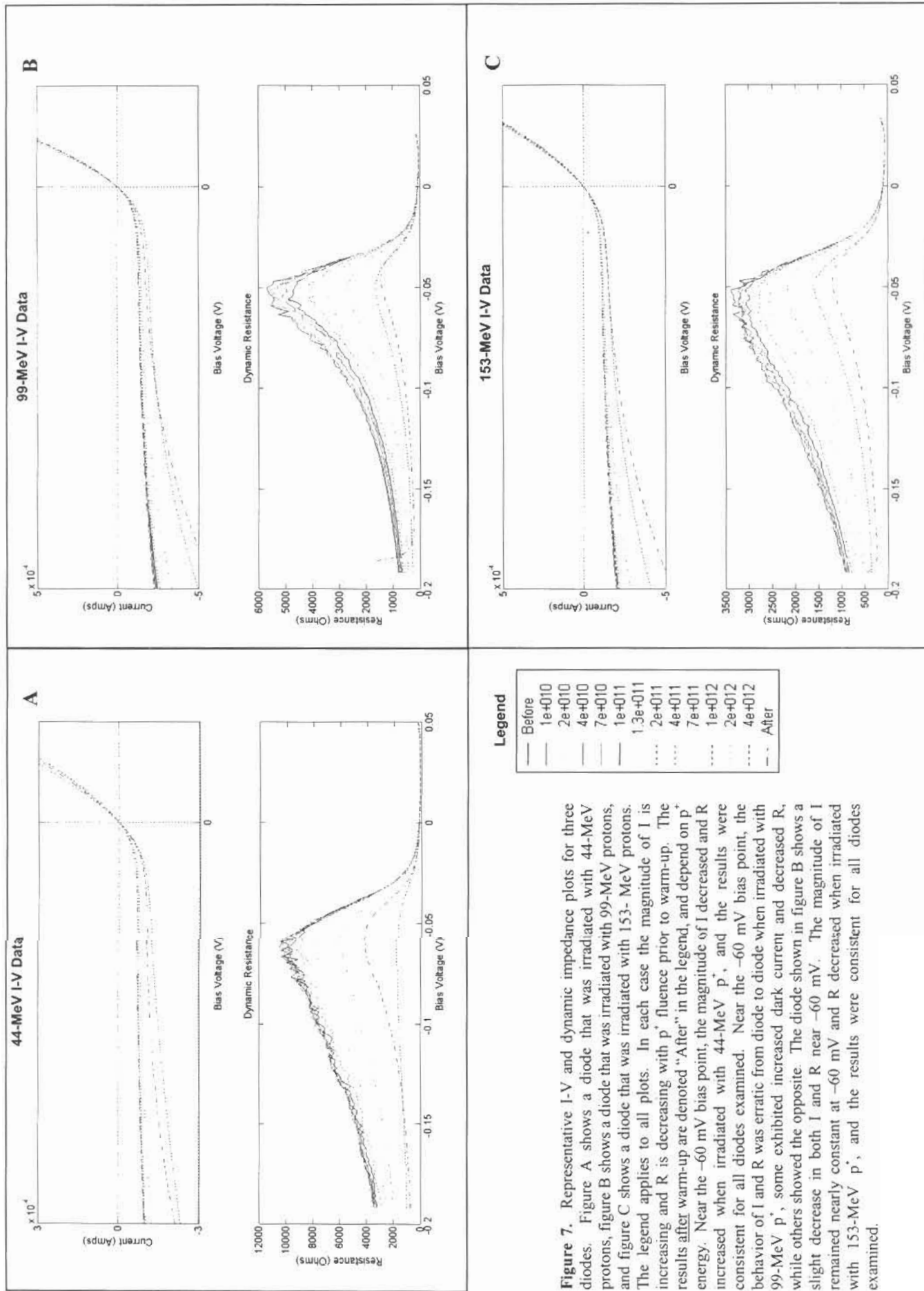


**Figure 7.** Representative I-V and dynamic impedance plots for three diodes. Figure A shows a diode that was irradiated with 44-MeV protons, figure B shows a diode that was irradiated with 99-MeV protons, and figure C shows a diode that was irradiated with 153-MeV protons. The legend applies to all plots. In each case the magnitude of I is increasing and R is decreasing with p<sup>+</sup> fluence prior to warm-up. The results after warm-up are denoted "After" in the legend, and depend on p<sup>+</sup> energy. Near the -60 mV bias point, the magnitude of I decreased and R increased when irradiated with 44-MeV p<sup>+</sup>, and the results were consistent for all diodes examined. Near the -60 mV bias point, the behavior of I and R was erratic from diode to diode when irradiated with 99-MeV p<sup>+</sup>, some exhibited increased dark current and decreased R, while others showed the opposite. The diode shown in figure B shows a slight decrease in both I and R near -60 mV. The magnitude of I remained nearly constant at -60 mV and R decreased when irradiated with 153-MeV p<sup>+</sup>, and the results were consistent for all diodes examined.

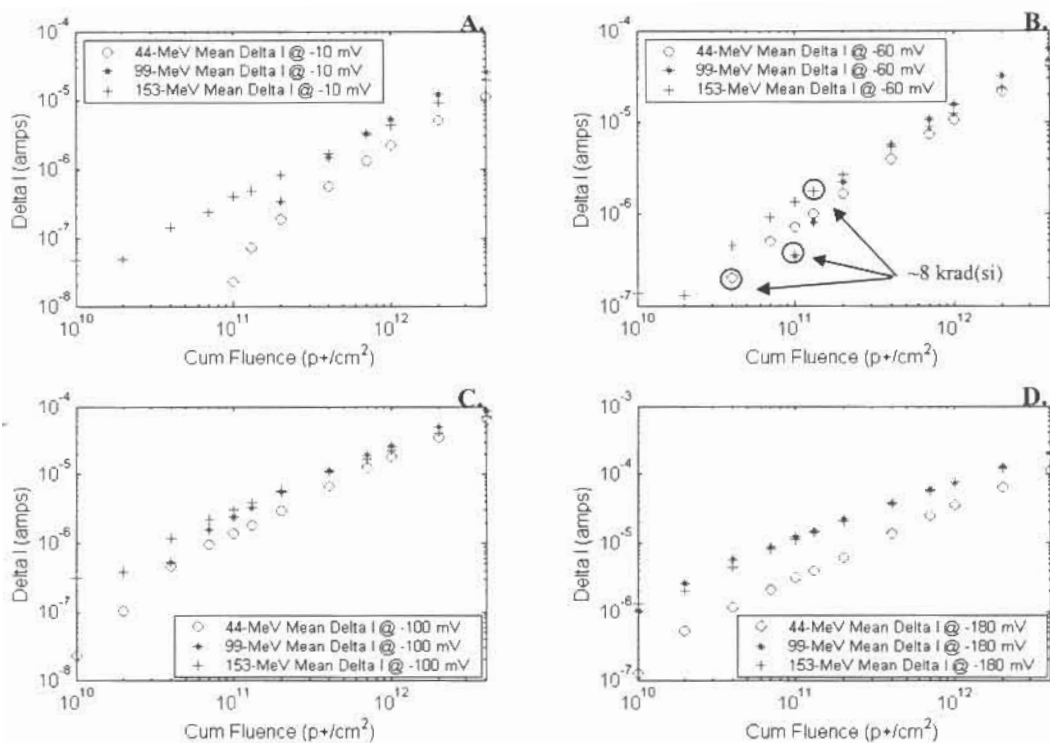


**Figure 8.** Mean increase in reverse biased dark current from all detectors tested at 44, 99, and 153-MeV. Current increase is shown for A. 10 mV, B. 60 mV, C. 100 mV, and D. 180 mV reverse bias. The circled points in plot B indicate the 7-year CrIS lifetime total radiation dose requirement, for all three proton energies, when operating at the nominal -60 mV bias.

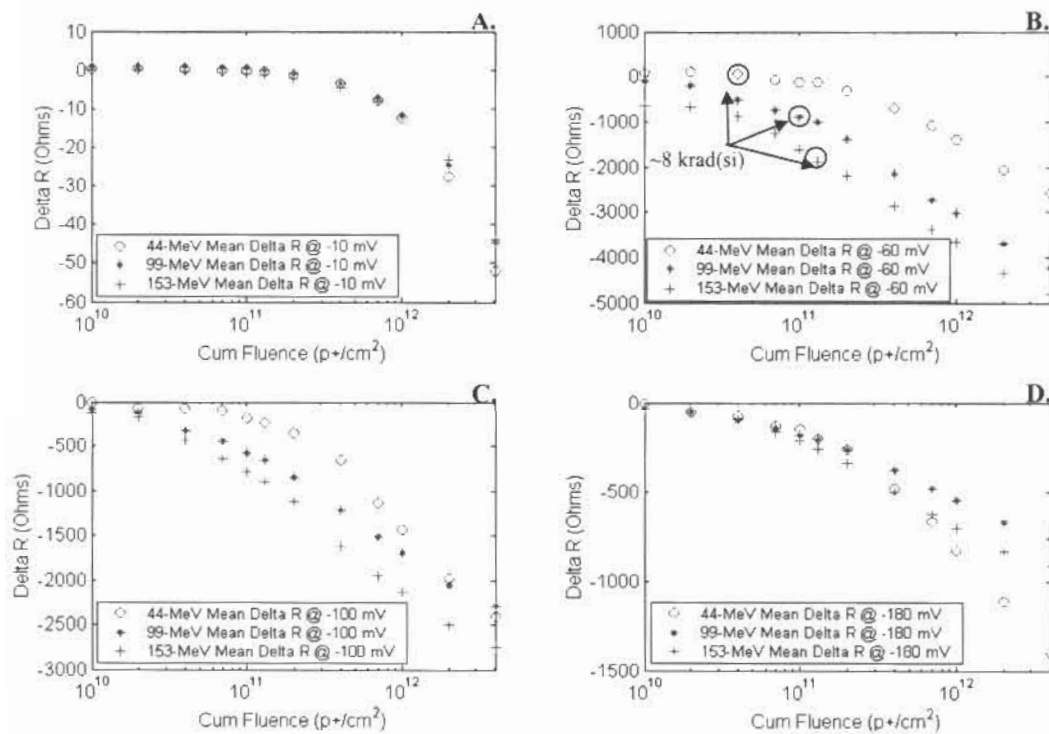


**Figure 9.** Mean decrease in reverse biased dynamic impedance for all detectors tested at 44, 99, and 153-MeV. Impedance decrease is shown for A. 10 mV, B. 60 mV, C. 100 mV, and D. 180 mV reverse bias. The circled points in plot B indicate the 7-year CrIS lifetime total radiation dose requirement, for all three proton energies, when operating at the nominal -60 mV bias.

#### 4.0 DISCUSSION OF RESULTS

There are many intriguing characteristics of the dark current and dynamic impedance dependence on proton energy, fluence, and bias voltage. The data suggests that the primary mechanism that increases dark current following high-energy proton bombardment of the CrIS detectors is tunneling. The dark current increase was far greater with high reverse bias voltage (100-200  $\mu$ Amps after  $4 \times 10^{12}$   $p^+/cm^2$ ), than near zero bias (10-30  $\mu$ Amps after  $4 \times 10^{12}$   $p^+/cm^2$ ). There appears to be energy and bias dependent fluence thresholds for dark current increase and dynamic impedance decrease. Below threshold the current and impedance are unchanged, or slightly improved (note that these points do not appear on the logarithmic plots in figure 8). Above threshold the change in dark current is approximately linear with fluence, while the dynamic impedance has a logarithmic dependence. The current and impedance dependence on proton energy varies depending on bias and fluence. It is unknown how much of the observed results are due to lot variations of the detectors, but it could be a factor.

At CrIS nominal -60 mV reverse bias voltage (figure 8B) the dark current initially decreased slightly with fluence, using 44 and 99-MeV protons. After the threshold fluence,  $\sim 0.4 - 2 \times 10^{11}$   $p^+/cm^2$ , the change in dark current became approximately linear with fluence. Using 153-MeV protons, the current was approximately linear with fluence above  $2 \times 10^{10}$   $p^+/cm^2$ . The change in dark current had a small dependence on proton energy above threshold, with 99-MeV protons causing the largest change in dark current, and 44-MeV protons causing the smallest change in dark current. The threshold for dynamic impedance reduction (figure 9B) was approximately  $2 \times 10^{11}$   $p^+/cm^2$  using 44-MeV protons, and  $4 \times 10^{11}$   $p^+/cm^2$  using 99 and 153-MeV protons. The dynamic impedance was more sensitive to 153-MeV protons, and least sensitive to 44-MeV protons.

To assess the effect of high-energy protons on the 7-year CrIS detection limited noise performance, consider equation 1.1 and the following baseline parameters:  $I_d = 1.5 \times 10^{-4}$  Amps,  $I_{s\_ph} + I_{b\_ph} = 5.65 \times 10^{-4}$ ,  $R_d = 6500 \Omega$ ,  $\alpha = 2 \times 10^{-5}$ ,  $f = 7500$  Hz (corresponding to  $750 \text{ cm}^{-1}$ ), and  $V_{pa} = 5 \text{ nV/Hz}^{1/2}$ . Figure 10 plots the percentage increase in NESR as a function of proton fluence for each of the three energies tested.

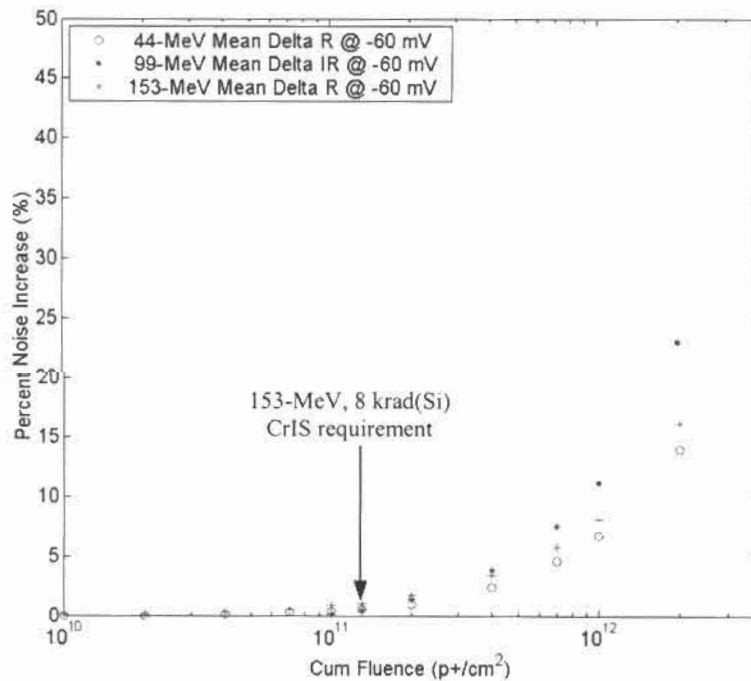


**Figure 10.** NESR (noise) increase at 7500 Hz ( $750 \text{ cm}^{-1}$ ) following exposure of CrIS LWIR  $Hg_{1-x}Cd_xTe$  photodiodes to 44, 99, and 153-MeV protons, as a function of fluence ( $p^+/cm^2$ ). The arrow shows the maximum expected noise increase for the CrIS 8 krad(Si) requirement, less than 1%.

The noise increase has very little energy dependence below  $4 \times 10^{11} \text{ p}^+/\text{cm}^2$ . The worst-case CrIS 8krad(Si) exposure was using 153-MeV protons at  $1.2 \times 10^{11} \text{ p}^+/\text{cm}^2$ . The noise increase at this point was approximately 0.75%. The maximum noise increase observed was approximately 47%, occurring at  $4 \times 10^{12} \text{ p}^+/\text{cm}^2$  using 99-MeV protons, corresponding to 372 krad(Si). Since the data showed a small decrease in dark current following approximately 96 hours at room temperature, annealing could reduce some of the noise induced by high proton radiation doses. The inherent assumption in this analysis is that quantum efficiency (QE) remains constant following proton irradiation. The most likely mechanism for reduced QE is a shortening of the minority carrier lifetime. This however, would also increase the diffusion dark current. Since there is no appreciable increase in diffusion current following 8krad(Si) irradiation, there is probably no effect on QE. At higher dose levels, the QE may be affected.

## 5.0 CONCLUSION

This study confirms that radiation induced damage on the CrIS LWIR  $\text{Hg}_{1-x}\text{Cd}_x\text{Te}$  detectors following a seven-year mission will not significantly degrade performance. The dominant mechanism for increased CrIS NESR was increased dark current causing higher 1/f noise contribution to the total system noise. Tunneling appears to be the primary cause of the dark current increase. Conservatism has been built into the analysis; conservative estimates of the amount of shielding provided by the sensor structure, with an additional 100% margin, ensured an accurate prediction of maximum possible noise growth. Larger noise growth was observed at higher doses, however the CrIS detectors will not be exposed to that level of radiation. The threshold for significant growth was approximately  $4 \times 10^{11} \text{ p}^+/\text{cm}^2$  independent of proton energy. Applications, which expect this level of radiation, or higher, should consider

## 6.0 ACKNOWLEDGEMENTS

This work was sponsored by the Department of the Air Force under Air Force Contract No. F19628-00-C-0002.

## 7.0 REFERENCES

1. K. Schwantes, D.Cohen, P. Mantica, R. Glumb, *SPIE Proceedings*, p. 456-463, Vol. 4486, 2002
2. R. J. Glumb, D.C. Jordan, P. Mantica, *SPIE Proceedings*, p. 411-424, Vol. 4486, 2002
3. A.I. D'Souza, L.C. Dawson, E.J. Anderson, A.D. Markum, W.E. Tennant, L.O. Bubulac, M. Zandian, J.G. Pasko, W.V. McLevige, D.D. Edwall, *J. Electron. Mater.* 26, 656 (1997).
4. J.M. Arias, J.G. Pasko, M. Zandian, S.H. Shin, G. M. Williams, L.O. Bubulac, R.E. DeWames, W.E. Tennant, *Appl. Phys. Lett.* Vol. 62, p. 976 (1993).
5. H. Holloway, *J. Appl. Phys.*, Vol. 49, p. 4264 (1978).
6. P.S. Wijewarnasuriya, M. Zandian, D.B. Young, J. Waldrop, D.D. Edwall, W.V. McLevige, J. Arias, A.I. D'Souza, *J. Electron. Mater.* Vol. 28, p. 649 (1999).
7. S.Tobin, et al, *IEEE-Transactions-on-Electron-Devices*, p.43-8, Vol.ED-27, no.1; Jan. 1980
8. A.I. D'Souza, M.G. Stapelbroek, S.A. Masterjohn, P.S. Wijewarnasuriya, R.E. DeWames, D.L. Smith, J. Ehlert, , *SPIE Proceedings*, Vol. 4820, 2002
9. M.B. Reine. Ed. P. Capper and C.T. Elliot, p. 331-376. Kluwer Academic Publishers. Boston. 2001.

- 
10. D. Rosenfeld, G. Bahir, *IEEE Trans Elec Dev.*, p. 1638 –1645, Vol. 39 Num. 7, July 1992.
  11. NPOESS General Instrument Interface Document (DRAFT), August 6, 2001.
  12. J.F. Janni. TR No. AFWL-TR-65-150, September, 1966.

NPOESS IPO/ADA  
Capt Smith

# Proton Irradiations of Large Area $Hg_{1-x}Cd_xTe$ Photovoltaic Detectors for the Cross-track Infrared Sounder

M.W. Kelly<sup>a</sup>, E.J. Ringdahl<sup>a</sup>, A.I. D'Souza<sup>b</sup>, S.D. Luce<sup>c</sup>, and E.W. Cascio<sup>d</sup>

<sup>a</sup> MIT Lincoln Laboratory, 244 Wood St., Lexington, MA 02420

<sup>b</sup> DRS Sensors & Targeting Systems, 3400 Miraloma Ave., Anaheim, CA 92806

<sup>c</sup> ITT Aerospace/Communications Division, Ft. Wayne, IN 46801

<sup>d</sup> Harvard Cyclotron Lab, 44 Oxford St., Cambridge, MA 02138

DIRECTORATE FOR FREEDOM OF INFORMATION  
AND SECURITY REVIEW  
DEPARTMENT OF DEFENSE

CLEARED  
FOR OPEN PUBLICATION

JUN 27 2002 14

02 - 0385  
SAR/PAS document

Call 887-3222/887-8932  
for pickup or return to 5D227

## ABSTRACT

The effect of radiation on  $Hg_{1-x}Cd_xTe$  photodiodes is an important parameter to understand when determining the long-term performance limitations for the Cross-track Infrared Sounder (CrIS), a Fourier Transform interferometric sensor that will fly as part of the National Polar-orbiting Operational Environmental Satellite System (NPOESS). The CrIS sensor uses relatively large area photovoltaic detectors, 1 mm in diameter. Each p-on-n  $Hg_{1-x}Cd_xTe$  photodiode consists of MBE grown, n-type material on lattice matched CdZnTe, with arsenic implantation used to form the junction. A 1mm diameter detector is achieved by using a lateral collection architecture. Solar, and trapped protons are a significant source of radiation in the NPOESS 833 km orbits. We irradiated 22 LWIR detectors with protons at the Harvard Cyclotron Laboratory (HCL) and monitored the I-V performance and dynamic impedance of each detector. Three groups of detectors were irradiated with either 44, 99, or 153-MeV protons, each between  $1 \times 10^{10}$  -  $4 \times 10^{12}$  p<sup>+</sup>/cm<sup>2</sup> (total range ~ 0.7 - 690 krad(Si)). Several I-V data sets were collected within that fluence range at all three energies. All the detectors were warmed to room temperature for approximately 96 hours following the largest proton dose, re-cooled, and then re-characterized in terms of I-V performance and dynamic impedance. The total noise increase predicted for CrIS after 7-years in orbit is less than 1%.

**Keywords:**  $Hg_{1-x}Cd_xTe$  detectors, radiation tolerance, fourier transform spectrometer, remote sensing

## 1.0 BACKGROUND

A new era of operational polar-orbiting environmental satellites will be launched for the first time around 2008. NPOESS is a tri-agency venture between NOAA, NASA, and DoD, which merges civilian (POES) and defense (DMSP) polar meteorological satellite programs onto a single platform. The NPOESS satellites will eventually replace both two-satellite constellations. The NPOESS constellation will operate in an 833 km, 98.7° inclination, near sun-synchronous orbit. Currently three orbital planes are planned with 1330, 1730, and 2130 local equatorial ascending crossing times. In 1999, ITT Industries in Ft. Wayne, IN was awarded the contract to build CrIS. Meeting demanding noise performance requirements requires careful sensor design to achieve a detection-limited system.<sup>1,2</sup> In this work we quantify the effects caused by exposure of the CrIS long-wave infrared (LWIR) photodetectors to energetic protons; which is one mechanism that could affect system performance over the life of the instrument.

### 1.1. CrIS Detection Limited Noise Performance

The CrIS detectors are p-on-n double layer planar heterostructure (DLPH) diodes<sup>3</sup>. The DLPH architecture<sup>4</sup> reduces surface generation-recombination and tunneling currents by incorporating a buried narrow-bandgap active layer in the DLPH architecture. MBE is used to grow n-type  $Hg_{1-x}Cd_xTe$  on lattice matched CdZnTe. The wafer material is grown with wider bandgap cap layers. The required 1000  $\mu$ m diameter detectors were manufactured using the lateral collection diode (LCD) architecture<sup>5</sup> to reduce the probability of a

02-S-1897



performance degrading defects<sup>6</sup> intersecting the p/n junction. The 1000  $\mu\text{m}$  diameter detector consists of 2298 p-type implants tied together at the metal level to form a single large detector. The detector geometry is back-illuminated; i.e. photons traverse the transparent CdZnTe and impinge on the absorbing n-type material, opposite the p/n junction. Absorbed photons create electron-hole pairs. Minority carriers generated within a diffusion length of the junction contribute to current flow. Figure 1 shows the LCD detector and back-illuminated DLPH architecture.

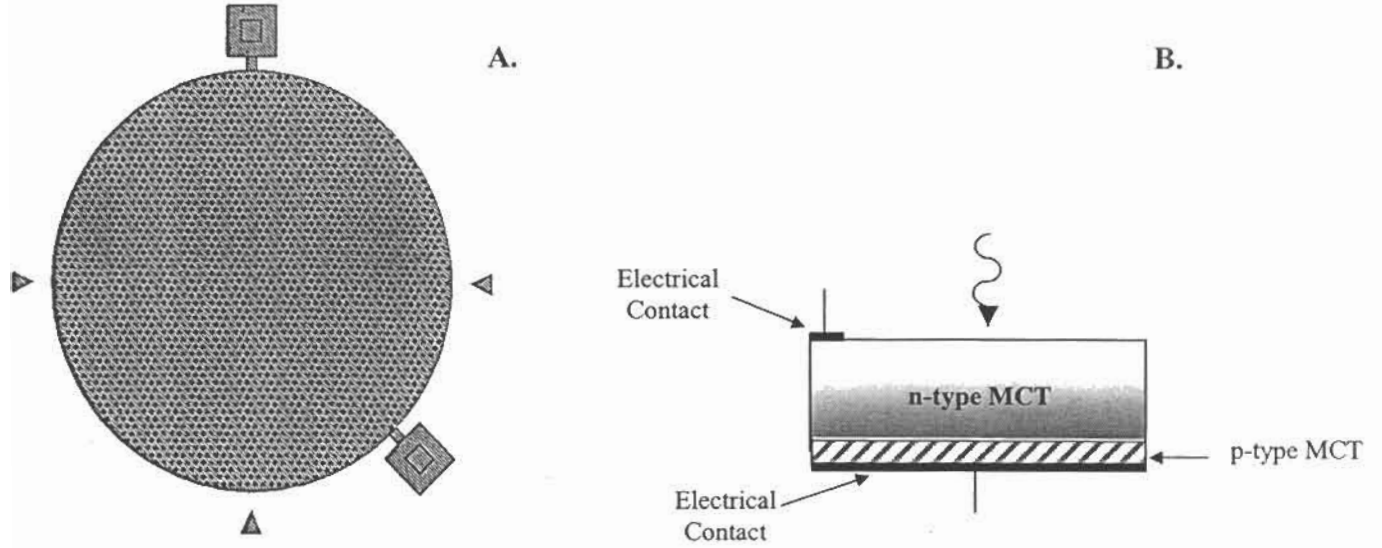


Figure 1. A. 1 mm CrIS diodes consisting of 2298 small implants, tied together in a metal layer. B. Back-illuminated p on n photovoltaic detector

The detection-limited performance of the CrIS sensor can be examined by considering the mechanisms for noise within the detection circuit. The noise equivalent spectral radiance (NESR) is directly proportional to the total noise current,  $I(f)_T$ . The diodes are operated relatively warm;  $T = 81\text{K}$  (LW) and  $T = 98\text{K}$  (MW & SW), and reverse biased at  $V_b \approx -60\text{mV}$ . The bias is optimized to present the highest possible source impedance to the preamplifier. A resistive transimpedance preamplifier provides enough gain to render the noise in down-stream electronics negligible. The dominant noise mechanisms are: dark current ( $I_d$  Amps) shot noise, photocurrent ( $I_{s\_ph} + I_{b\_ph}$  Amps) shot noise,  $1/f$  noise in the diode, and amplifier noise. The total noise current in terms of  $\text{A}/\text{Hz}^{1/2}$  can be written:

$$I(f)_T = \sqrt{2qI_d + 2q(I_{s\_ph} + I_{b\_ph}) + \frac{\alpha^2 I_d^2}{f} + \left(\frac{V_{pa}}{R_d}\right)^2} \quad (1.1)$$

Where  $q$  is the electronic charge unit,  $1.6 \times 10^{-19}$  Coulombs. Since CrIS is an AC coupled FTS, and time domain signal data is transformed into the frequency domain to recover the earth's radiant spectrum, the spectral content of the noise is an important consideration, particularly in the long-wave region of the spectrum. The  $1/f$  noise contribution is modeled according to [7]. The  $1/f$  noise is proportional to the dark current multiplied by a dimensionless quantity,  $\alpha$ , measured to be on the order of  $1-2 \times 10^{-5}$  for the CrIS LWIR detectors.<sup>8</sup> The preamplifier contribution to the total noise depends on the voltage noise of the input stage ( $V_{pa} \text{ V}/\text{Hz}^{1/2}$ ) and dynamic impedance of the detector ( $R_d \Omega$ ). It is determined by measuring  $-dV/dI$ . The input referred preamplifier noise current and  $1/f$  noise voltage in the CrIS signal band are expected to

be negligible, and were not included in equation 1. The dark current component in equation 1 is expected to have several components

$$I_d = I_o e^{\frac{-qV_b}{kT}} + I_o + I_T + I_{DEF} \quad (1.2)$$

Where  $I_{DEF}$  are lattice defect related current mechanisms, and  $I_T$  is band-to-band tunneling current. Defect related current mechanisms include Shockley-Read diffusion, surface generation-recombination, depletion region generation-recombination, and trap-assisted tunneling.<sup>9,10</sup> At the beginning of life the CrIS detectors can achieve near thermal diffusion limited dark current. The present study seeks to quantify how defects caused by protons interacting with the detector material increase the dark current, and how the noise performance of the CrIS may be affected. Although not characterized in this study, the quantum efficiency could also be affected by the proton irradiation. This issue will be discussed in section 4 of this paper.

## 1.2 CrIS Radiation Environment

The radiation environment for the CrIS has been defined in the NPOEES General Instrument Interface Document<sup>11</sup> (GIID). The sensor must be capable of meeting all performance parameters over a seven-year mission when exposed to the trapped proton, solar flare proton, and trapped electron spectra shown in figure 2. Additionally a factor of two design margin is mandated. The total dose requirement for

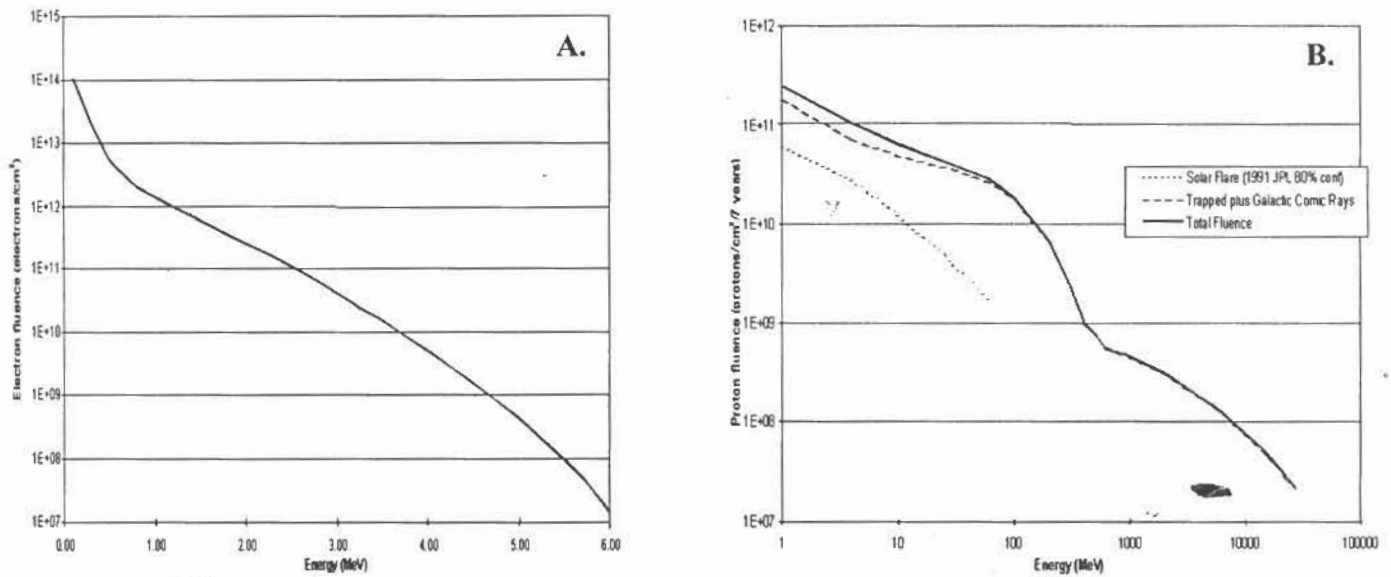


Figure 2. A. Electron and B. Proton environment as specified in the GIID

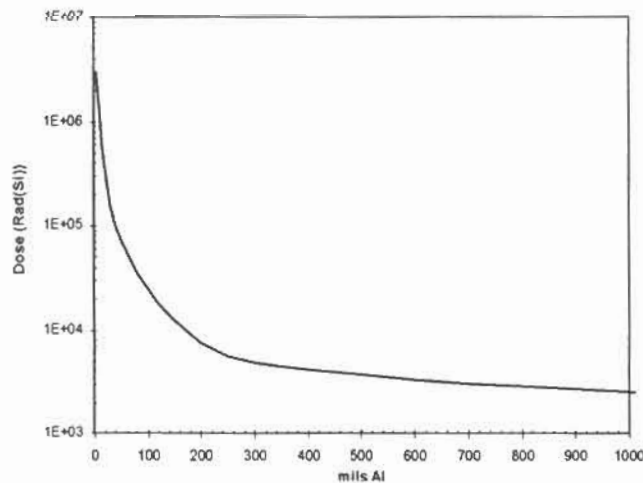


Figure 3. Total dose environment as specified in the GIID

Table 1. Total dose environment as specified in the GIID broken into source components

Shielding Mils (AL)	Trapped Protons Rad(Si)/7 Yr	Trapped Electrons Rad(Si)/7 Yr	Solar Flare Protons Rad(Si)/7 Yr	Total Rad(Si)/ Yr
100	6.30 E03	1.81 E04	1.56 E03	2.62 E04
200	4.79 E03	2.06 E03	7.12 E02	7.56 E03
400	3.67 E03	6.76 E01	4.06 E02	4.14 E03
600	3.05 E03	4.35 E01	0.00 E00	3.09 E03
1000	2.25 E03	3.04 E01	0.00 E00	2.28 E03

internal electrical components is plotted in figure 3 as a function of equivalent shielding thickness. The contribution from protons and electrons is delineated for several shield thickness values in table 1.

The CrIS detectors are positioned within the FPA module and mounted to a passive radiator, which has a clear view to space. The FPA module was analyzed in two planes (Y-Z and X-Z) for a first order estimate of the equivalent aluminum shielding thickness provided by the sensor. Each plane was then divided into four 90-degree. The quadrant that is most susceptible to radiation is the space-viewing quadrant identified in the Y-Z Plane. This 90-degree quadrant was then broken down into six 15-degree

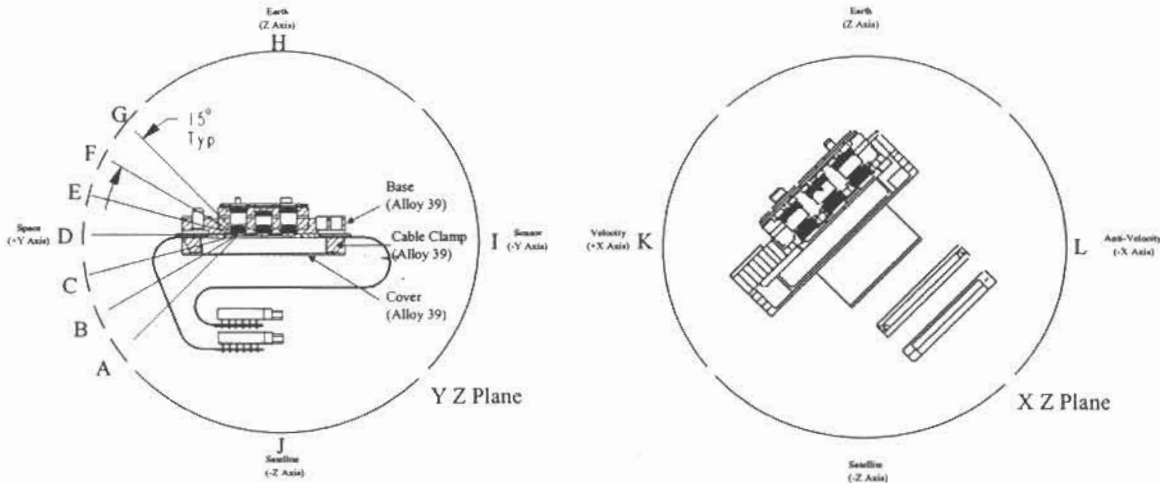


Figure 4. CrIS detector assembly and the geometrical coordinates identified for radiation shielding analysis

increments, identified "A" thru "G" to estimate the total radiation shielding that exists in this quadrant. Figure 4 shows the detector assembly and the geometrical coordinates identified for analysis. The materials and respective densities that are present within the module design are listed in table 2.

Table 2. Relevant materials used in the CrIS sensor

Material	Density g/cm <sup>3</sup>	Density Ratio Material/Al
6061-T6 Aluminum	2.71	1
AlBeMet AM162	2.10	0.77
Beryllium SF200	1.85	0.68
Alloy 39	8.11	2.99
G10	1.80	0.66
Ceramic	2.49	0.92

The ratio of the material density to that of aluminum is also included. The effective aluminum shielding was determined by adding-up the thickness of each material within each quadrant angular field of view, extending from the outside of the sensor to the nearest detector, and multiplying by the density ratio. The analysis does not take into account manufacturing tolerances, the passive cooler honeycomb structure, MLI thermal blankets, or part plating. Table 3 summarizes each material thickness in each quadrant and the equivalent aluminum thickness. The minimum aluminum equivalent shielding thickness was 80-mils. The most sensitive Y-Z quadrant conservatively provides 500-mils shielding. The equivalent shielding averaged over the entire  $4\pi$  steradian sphere surrounding the detectors is even greater, however without much more proton stopping power according to figure 3. As a conservative estimate for this analysis, 8 krad(Si) radiation dose will be assumed for end-of-life performance estimates. This includes the required 2x GIID margin factor.

**Table 3.** Spreadsheet for effective aluminum shielding calculation

Quadrant	Part	Base Material	Thickness (in)	Ratio Factor	Effective Aluminum (in)
A	Emitter (Stage 4)	Be	0.043	0.68	0.029
	FPA Rear Cover	Alloy 39	0.017	2.99	0.051
					0.08
B	Emitter (Stage 4)	Be	0.043	0.68	0.029
	FPA Rear Cover	Alloy 39	0.017	2.99	0.051
					0.08
C	Emitter (Stage 4)	Be	0.043	0.68	0.029
	Cable Clamp	Alloy 39	0.156	2.99	0.466
					0.496
D	Emitter (Stage 4)	Be	0.043	0.68	0.029
	Flex Stiffener	G10	0.335	0.66	0.221
	CMLB	Ceramic	0.26	0.92	0.239
					0.49
E	Emitter (Stage 4)	Be	0.25	0.68	0.17
	FPA Base	Alloy 39	0.5	2.99	1.495
					1.665
F	Emitter (Stage 4)	Be	0.375	0.68	0.255
	Emitter (Stage 3) ~	Be	0.625	0.68	0.425
	Housing (Stage 3)	Al	0.375	1	0.375
	Housing (Stage 4)	Al	0.625	1	0.625
	FPA Base	Alloy 39	0.375	2.99	1.121
					2.801
G	Exceeds 1 inch of Aluminum equivalent material shielding thickness				
H	Exceeds 1 inch of Aluminum equivalent material shielding thickness				
I	Exceeds 1 inch of Aluminum equivalent material shielding thickness				
J	Exceeds 1 inch of Aluminum equivalent material shielding thickness				
K	Thermal Shield	Al	0.02	1	0.02
	Vac Hsg Cover	Al	0.032	1	0.032
	Vac Hsg (Stage 1)	AlBeMet	0.078	0.77	0.06
	Flexure Shield (Stage 2)	Al	0.02	1	0.02
	Flexure Bracket (Stage 2)	AlBeMet	0.06	0.77	0.046
	Radiator (Stage 2)	AlBeMet	0.156	0.77	0.12
	Shield (Stage 3)	Al	0.02	1	0.02
	Housing (Stage 3)	Al	0.125	1	0.125
	FPA Rear Cover	Alloy 39	0.017	2.99	0.051
					0.494
L	Thermal Shield	Al	0.02	1	0.02
	Vac Hsg Cover	Al	0.032	1	0.032
	Vac Hsg (Stage 1)	AlBeMet	0.078	0.77	0.06
	Vac Hsg (Stage 1)	AlBeMet	0.156	0.77	0.12
	Flexure Shield (Stage 2)	Al	0.02	1	0.02
	Flexure Bracket (Stage 2)	AlBeMet	0.06	0.77	0.046
	Radiator (Stage 2)	AlBeMet	0.078	0.77	0.06
	Shield (Stage 3)	Al	0.02	1	0.02
	Housing (Stage 3)	Al	0.06	1	0.06
	Housing (Stage 4)	Al	0.05	1	0.05
	Housing (Stage 4)	Al	0.06	1	0.06
	FPA Rear Cover	Alloy 39	0.017	2.99	0.051
					0.599

## 2.0 EXPERIMENTAL PROCEDURE

Risk reduction activities for CrIS involved fabricating detectors in all three channels for engineering unit (EU) demonstrations. The EUs focused on demonstrating all technical specifications needed to meet performance requirements. The LWIR detectors were the most challenging devices to fabricate, and as such produced more spares than the MWIR or SWIR EUs, i.e. rejected detectors that met nearly all performance requirements. There were twenty-two LWIR detectors available for destructive radiation testing. The devices were mounted into standard 64-pin leadless chip carriers (LLCC). The twenty-two detectors were divided into three groups with eight, eight, or six viable detectors mounted in

each LLCC. The LLCCs were mounted into a socket mechanically constrained with a G10 curb and clamped into place with a 100-mil aluminum cover. Figure 5 shows the assembly.

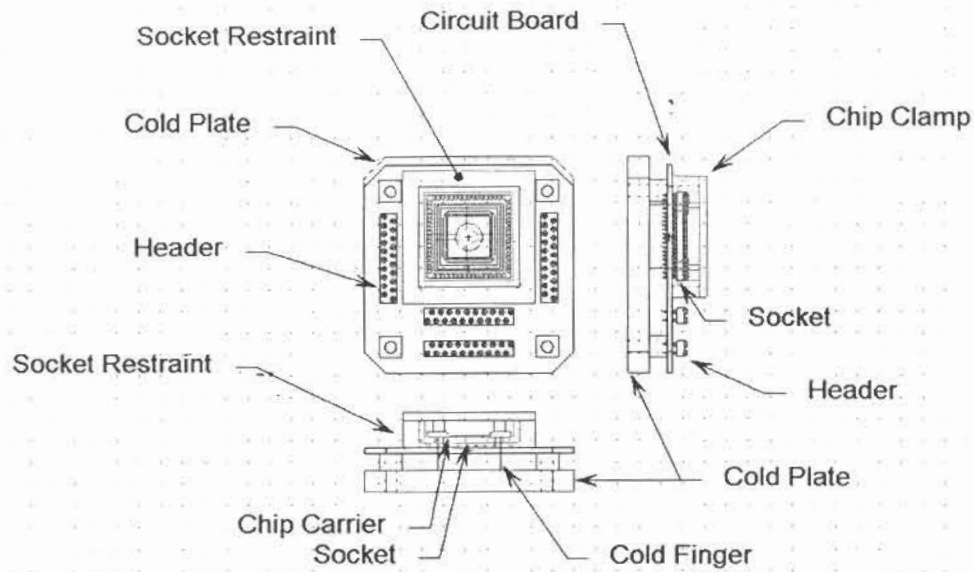


Figure 5. 64-pin LLCC socket assembly and cold finger for mounting the detectors into the LN2 dewar.

The circuit board was mounted through standoffs onto a copper-plate/cold-finger assembly which was clamped directly to the cold base of a liquid nitrogen dewar. The cover was sufficiently cold for dark I-V

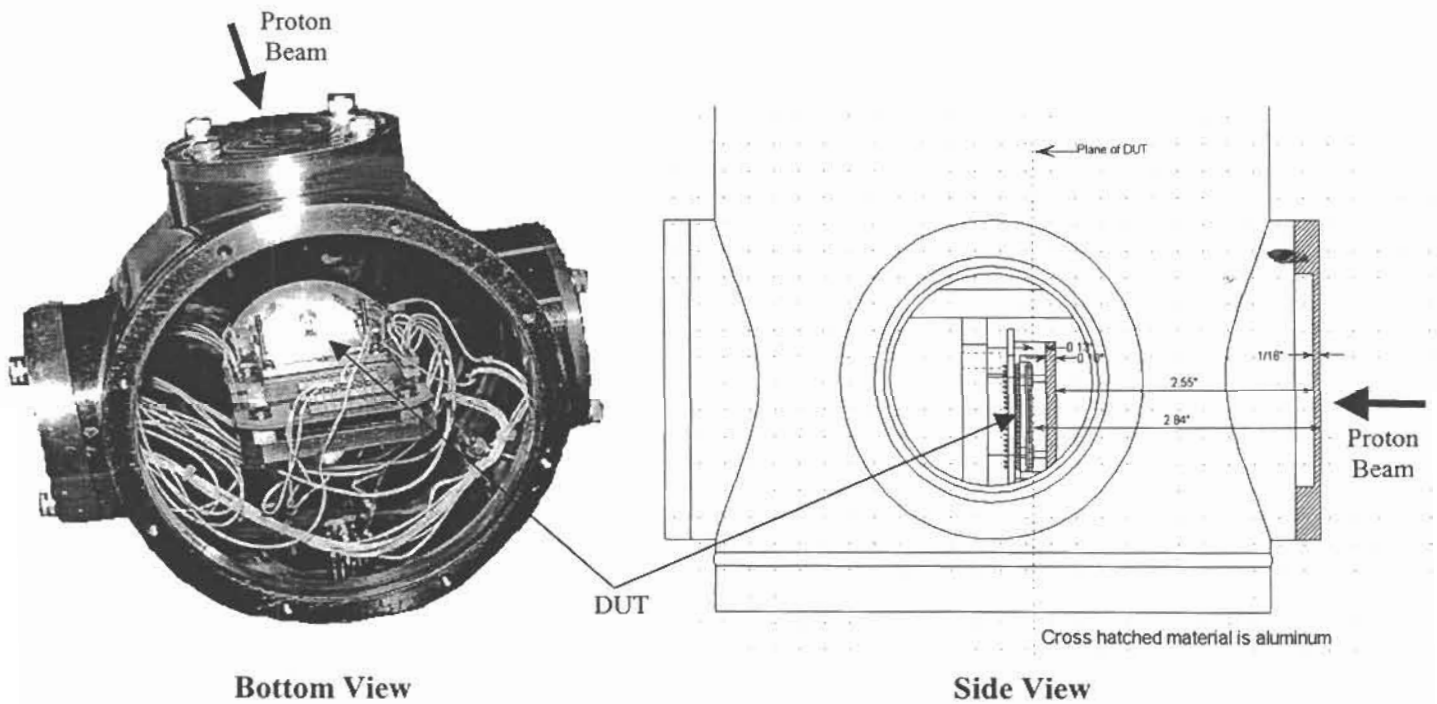


Figure 6. LN2 dewar assembly with cold mechanical assembly showing geometry and shielding used for proton irradiation

measurements. A platinum resistor was epoxied directly onto the cold finger to monitor temperature of the device under test (DUT). The dewar was evacuated and the DUT was maintained at approximately 78K for all proton irradiations and I-V measurements. A 62.5-mil aluminum cover was used to close the dewar port normal to the proton beam.

The facility used for irradiations was the Harvard Cyclotron Lab, in Cambridge Massachusetts. The accelerator is a synchrocyclotron that produces a fixed energy proton beam of 158.5-MeV. Introducing energy degraders into the beamline produces lower energy beams. The degraders also scatter the focused beam to uniformly cover any necessary field size. The degraders were composed of an acrylic resin, lead, or a combination of both materials, depending on the amount of absorption and/or scattering needed. The fluence was monitored during irradiations with a transmission (thin foil) ion chamber installed in the beam collimator, downstream of the degraders. Before the irradiation the signal produced in this ion chamber was calibrated to a faraday cup placed at the position of the target. Each of the three DUTs was exposed to only a single fixed proton energy beam: 44, 99, or 153-MeV between  $10^{10} - 4 \times 10^{12} \text{ p}^+/\text{cm}^2$ . The proton energy and fluence was initially calibrated external to the dewar. The beam parameters were then calculated at the DUT using the geometry and position of the aluminum dewar cover and LLCC cold clamp preceding the DUT in the beamline. Emulsion films were used in place of the DUT to verify the beam profile.

A laptop computer with a National Instruments PCMCIA 12-bit, 16-channel data acquisition (DAQ) card was used to collect data from up to nine detectors simultaneously. The DAQ analog voltage output was appropriately attenuated to sweep the bias on each diode in the DUT from -200 to +100 mV. A resistive transimpedance amplifier for each of nine channels converted the diode dark current to a voltage read by the DAQ.

### 3.0 RESULTS

An I-V data set was recorded just prior to each proton irradiation. The temperature was monitored during each measurement and remained stable to less than 0.2K. Table 4 shows the equivalent rad(Si) conversion used for the requirements analysis, and the 8-krad(Si) GIID requirement for the CrIS detectors.<sup>12</sup>

**Table 4.** Proton fluence to rad(Si) conversion and GIID requirement

Energy (MeV)	Conv. (rad(Si)/ ( $\text{p}^+/\text{cm}^2$ ))	8 krad(Si)Fluence Req ( $\text{p}^+/\text{cm}^2$ )
44	$1.7 \times 10^{-7}$	$4.7 \times 10^{10}$
99	$9.3 \times 10^{-8}$	$8.5 \times 10^{10}$
153	$6.9 \times 10^{-8}$	$1.2 \times 10^{11}$

Figure 7 shows a typical set of fourteen I-V curves for three diodes, one at each proton energy. The curves correspond to before the irradiation, after exposure to protons at various fluence intervals, and following approximately 96-hours of room temperature storage. In general, the change in dark current is small following lower fluence exposures, and increases as  $4 \times 10^{12} \text{ p}^+/\text{cm}^2$  is approached. The dynamic impedance at -60 mV bias decreased with increasing fluence, for all proton energy exposures. The I-V and dynamic impedance behavior following the room temperature annealing period varied depending on the group of diodes, and apparently proton energy the group was exposed, see figure 7. Quantitative details of each energy trial are presented below.

Figures 8 and 9 show the change in dark current and dynamic impedance respectively, at -10, -60, -100, and -180 mV reverse bias. Each data point is the mean of all detectors irradiated following each proton exposure at the specified proton energy. Absent data points in figure 8 A, B and C, for 44 and 99-MeV, at lower reverse bias, indicates zero or very slight decrease in the magnitude of dark current (on the order of  $10^{-7}$  Amps max). The data points corresponding to 8-krad(Si) are circled at the -60 mV CrIS bias point. At those points, dark current increased by approximately  $2 \times 10^{-7} - 2 \times 10^{-6}$  Amps, depending on proton energy. The higher energy protons induced more dark current than the lower. The dynamic impedance increase was between approximately 0 - 200  $\Omega$ . Again, the detectors were more sensitive to high-energy protons.



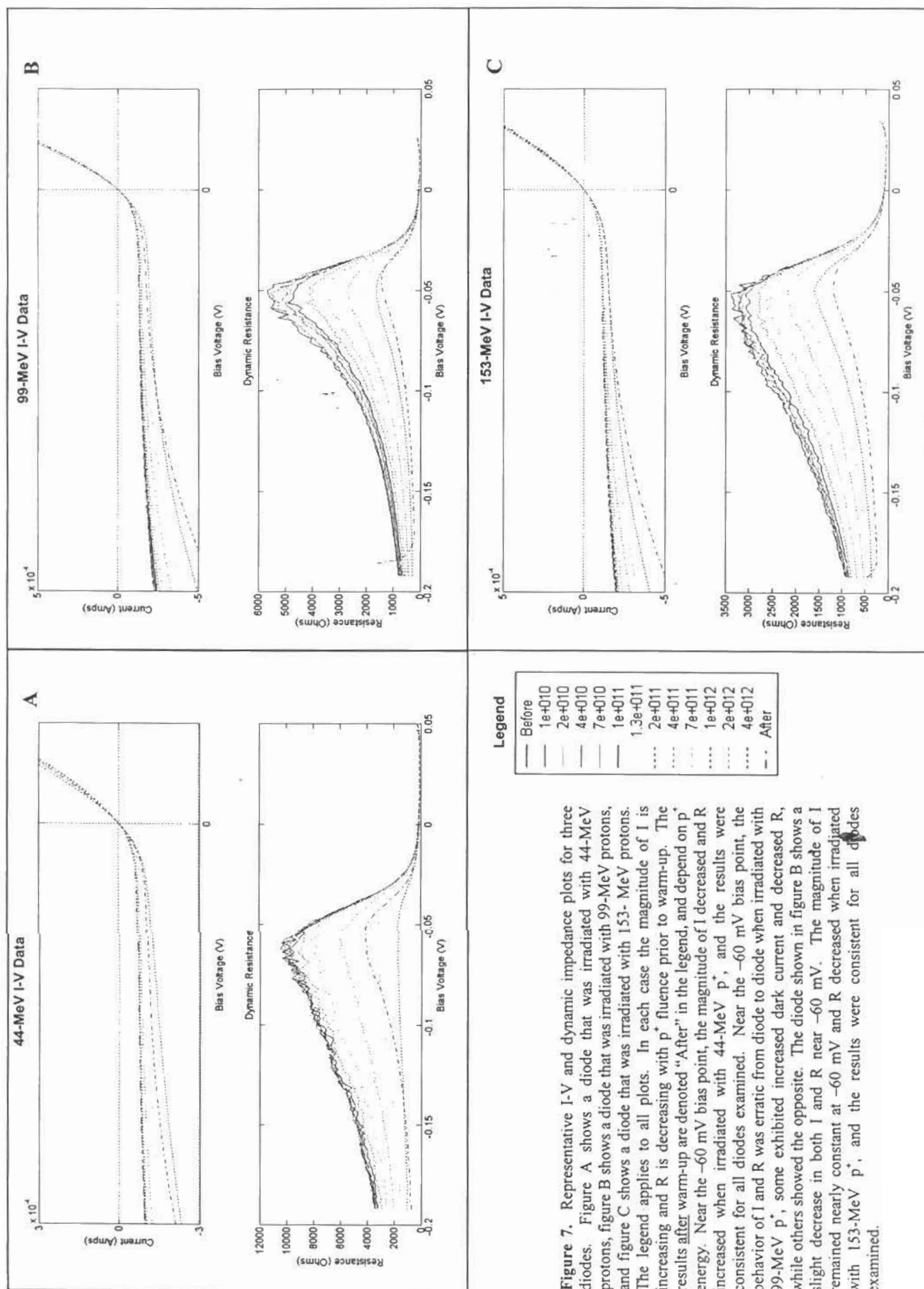


**Figure 7.** Representative I-V and dynamic impedance plots for three diodes. Figure A shows a diode that was irradiated with 44-MeV protons, figure B shows a diode that was irradiated with 99-MeV protons, and figure C shows a diode that was irradiated with 153-MeV protons. The legend applies to all plots. In each case the magnitude of I is increasing and R is decreasing with  $p^+$  fluence prior to warm-up. The results after warm-up are denoted "After" in the legend, and depend on  $p^+$  energy. Near the -60 mV bias point, the magnitude of I decreased and R increased when irradiated with 44-MeV  $p^+$ , and the results were consistent for all diodes examined. Near the -60 mV bias point, the behavior of I and R was erratic from diode to diode when irradiated with 99-MeV  $p^+$ , some exhibited increased dark current and decreased R, while others showed the opposite. The diode shown in figure B shows a slight decrease in both I and R near -60 mV. The magnitude of I remained nearly constant at -60 mV and R decreased when irradiated with 153-MeV  $p^+$ , and the results were consistent for all diodes examined.

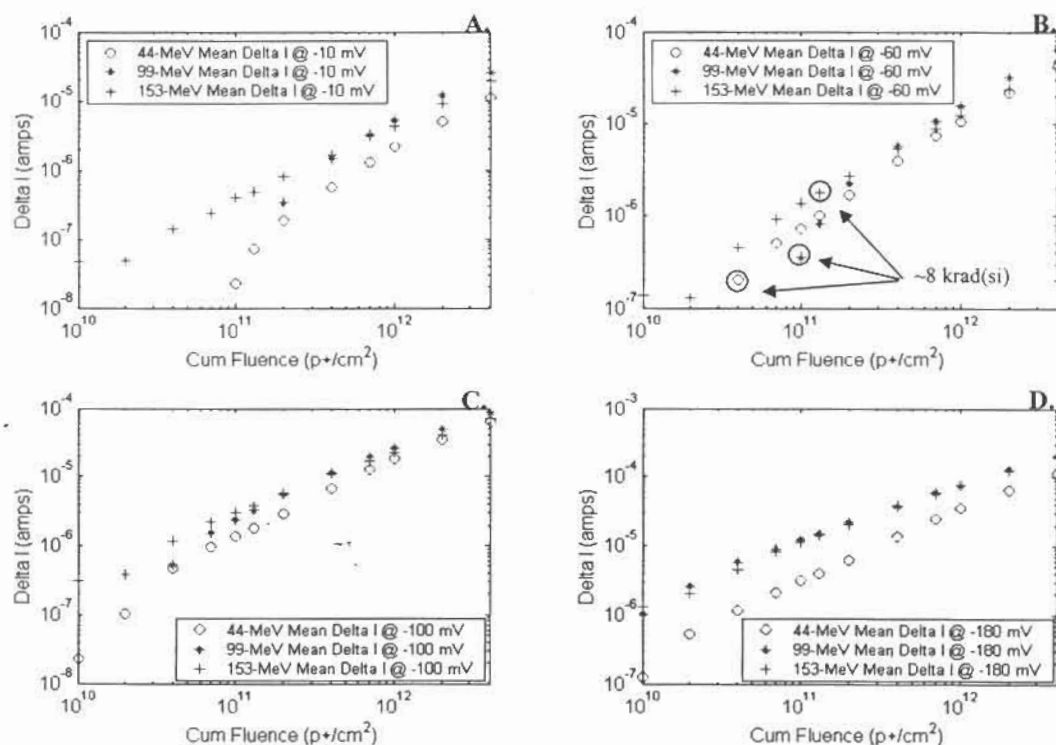


**Figure 8.** Mean increase in reverse biased dark current from all detectors tested at 44, 99, and 153-MeV. Current increase is shown for A. 10 mV, B. 60 mV, C. 100 mV, and D. 180 mV reverse bias. The circled points in plot B indicate the 7-year CrIS lifetime total radiation dose requirement, for all three proton energies, when operating at the nominal -60 mV bias.

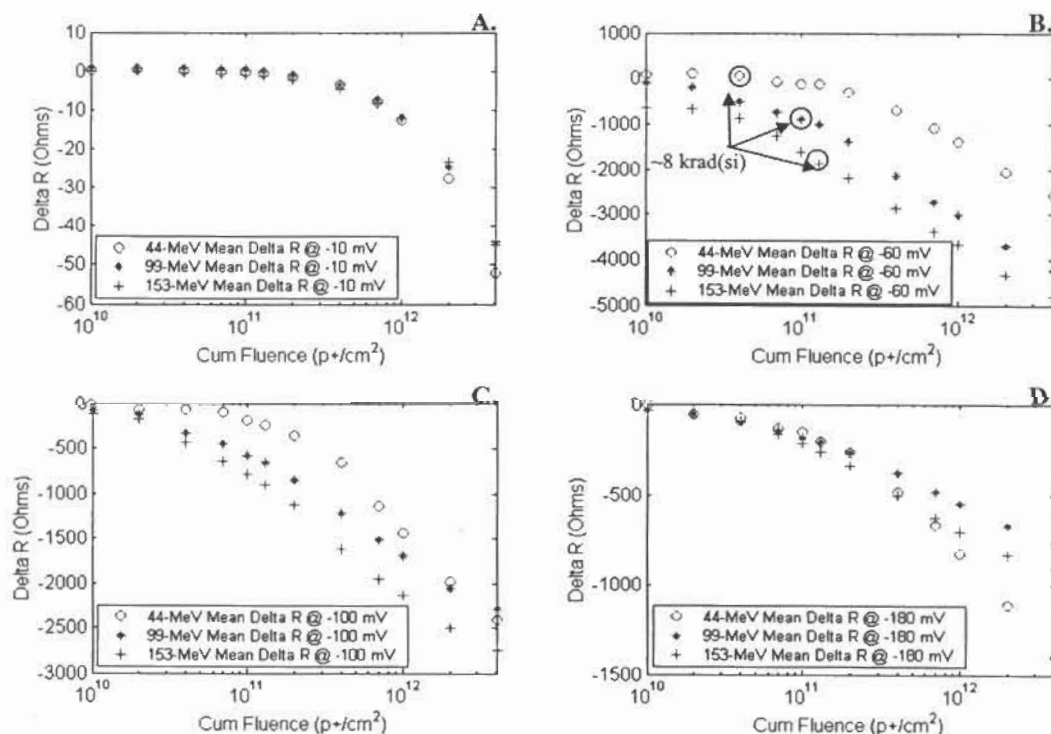


**Figure 9.** Mean decrease in reverse biased dynamic impedance for all detectors tested at 44, 99, and 153-MeV. Impedance decrease is shown for A. 10 mV, B. 60 mV, C. 100 mV, and D. 180 mV reverse bias. The circled points in plot B indicate the 7-year CrIS lifetime total radiation dose requirement, for all three proton energies, when operating at the nominal -60 mV bias.

#### 4.0 DISCUSSION OF RESULTS

There are many intriguing characteristics of the dark current and dynamic impedance dependence on proton energy, fluence, and bias voltage. The data suggests that the primary mechanism that increases dark current following high-energy proton bombardment of the CrIS detectors is tunneling. The dark current increase was far greater with high reverse bias voltage (100-200  $\mu$ Amps after  $4 \times 10^{12}$   $p^+/cm^2$ ), than near zero bias (10-30  $\mu$ Amps after  $4 \times 10^{12}$   $p^+/cm^2$ ). There appears to be energy and bias dependent fluence thresholds for dark current increase and dynamic impedance decrease. Below threshold the current and impedance are unchanged, or slightly improved (note that these points do not appear on the logarithmic plots in figure 8). Above threshold the change in dark current is approximately linear with fluence, while the dynamic impedance has a logarithmic dependence. The current and impedance dependence on proton energy varies depending on bias and fluence. It is unknown how much of the observed results are due to lot variations of the detectors, but it could be a factor.

At CrIS nominal -60 mV reverse bias voltage (figure 8B) the dark current initially decreased slightly with fluence, using 44 and 99-MeV protons. After the threshold fluence,  $\sim 0.4 - 2 \times 10^{11}$   $p^+/cm^2$ , the change in dark current became approximately linear with fluence. Using 153-MeV protons, the current was approximately linear with fluence above  $2 \times 10^{10}$   $p^+/cm^2$ . The change in dark current had a small dependence on proton energy above threshold, with 99-MeV protons causing the largest change in dark current, and 44-MeV protons causing the smallest change in dark current. The threshold for dynamic impedance reduction (figure 9B) was approximately  $2 \times 10^{11}$   $p^+/cm^2$  using 44-MeV protons, and  $4 \times 10^{11}$   $p^+/cm^2$  using 99 and 153-MeV protons. The dynamic impedance was more sensitive to 153-MeV protons, and least sensitive to 44-MeV protons.

To assess the effect of high-energy protons on the 7-year CrIS detection limited noise performance, consider equation 1.1 and the following baseline parameters:  $I_d = 1.5 \times 10^{-4}$  Amps,  $I_{s,ph} + I_{b,ph} = 5.65 \times 10^{-4}$ ,  $R_d = 6500$   $\Omega$ ,  $\alpha = 2 \times 10^{-5}$ ,  $f = 7500$  Hz (corresponding to  $750$   $cm^{-1}$ ), and  $V_{pa} = 5$  nV/Hz $^{1/2}$ . Figure 10 plots the percentage increase in NESR as a function of proton fluence for each of the three energies tested.

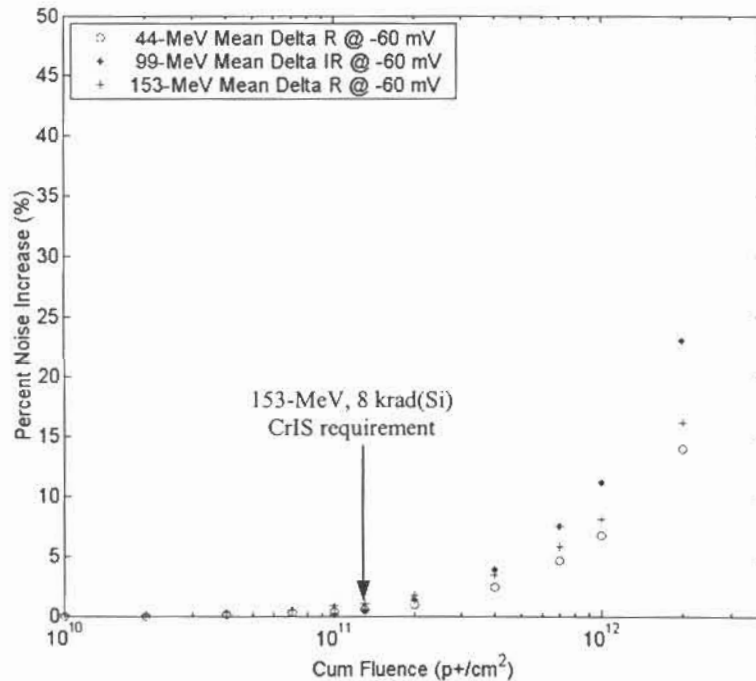


**Figure 10.** NESR (noise) increase at 7500 Hz ( $750$   $cm^{-1}$ ) following exposure of CrIS LWIR  $Hg_{1-x}Cd_xTe$  photodiodes to 44, 99, and 153-MeV protons, as a function of fluence ( $p^+/cm^2$ ). The arrow shows the maximum expected noise increase for the CrIS 8 krad(Si) requirement, less than 1%.

The noise increase has very little energy dependence below  $4 \times 10^{11} \text{ p}^+/\text{cm}^2$ . The worst-case CrIS 8krad(Si) exposure was using 153-MeV protons at  $1.2 \times 10^{11} \text{ p}^+/\text{cm}^2$ . The noise increase at this point was approximately 0.75%. The maximum noise increase observed was approximately 47%, occurring at  $4 \times 10^{12} \text{ p}^+/\text{cm}^2$  using 99-MeV protons, corresponding to 372 krad(Si). Since the data showed a small decrease in dark current following approximately 96 hours at room temperature, annealing could reduce some of the noise induced by high proton radiation doses. The inherent assumption in this analysis is that quantum efficiency (QE) remains constant following proton irradiation. The most likely mechanism for reduced QE is a shortening of the minority carrier lifetime. This however, would also increase the diffusion dark current. Since there is no appreciable increase in diffusion current following 8krad(Si) irradiation, there is probably no effect on QE. At higher dose levels, the QE may be affected.

## 5.0 CONCLUSION

This study confirms that radiation induced damage on the CrIS LWIR  $\text{Hg}_{1-x}\text{Cd}_x\text{Te}$  detectors following a seven-year mission will not significantly degrade performance. The dominant mechanism for increased CrIS NESR was increased dark current causing higher 1/f noise contribution to the total system noise. Tunneling appears to be the primary cause of the dark current increase. Conservatism has been built into the analysis; conservative estimates of the amount of shielding provided by the sensor structure, with an additional 100% margin, ensured an accurate prediction of maximum possible noise growth. Larger noise growth was observed at higher doses, however the CrIS detectors will not be exposed to that level of radiation. The threshold for significant growth was approximately  $4 \times 10^{11} \text{ p}^+/\text{cm}^2$  independent of proton energy. Applications, which expect this level of radiation, or higher, should consider

## 6.0 ACKNOWLEDGEMENTS

This work was sponsored by the Department of the Air Force under Air Force Contract No. F19628-00-C-0002.

## 7.0 REFERENCES

1. K. Schwantes, D.Cohen, P. Mantica, R. Glumb, *SPIE Proceedings*, p. 456-463, Vol. 4486, 2002
2. R. J. Glumb, D.C. Jordan, P. Mantica, *SPIE Proceedings*, p. 411-424, Vol. 4486, 2002
3. A.I. D'Souza, L.C. Dawson, E.J. Anderson, A.D. Markum, W.E. Tennant, L.O. Bubulac, M. Zandian, J.G. Pasko, W.V. McLevige, D.D. Edwall, *J. Electron. Mater.* 26, 656 (1997).
4. I.M. Arias, J.G. Pasko, M. Zandian, S.H. Shim, G. M. Williams, L.O. Bubulac, R.E. DeWames, W.E. Tennant, *Appl. Phys. Lett.* Vol. 62, p. 976 (1993).
5. H. Holloway, *J. Appl. Phys.*, Vol. 49, p. 4264 (1978).
6. P.S. Wijewarnasuriya, M. Zandian, D.B. Young, J. Waldrop, D.D. Edwall, W.V. McLevige, J. Arias, A.I. D'Souza, *J. Electron. Mater.* Vol. 28, p. 649 (1999).
7. S.Tobin, et al, *IEEE-Transactions-on-Electron-Devices*, p.43-8, Vol.ED-27, no.1; Jan. 1980
8. A.I. D'Souza, M.G. Stapelbroek, S.A. Masterjohn, P.S. Wijewarnasuriya, R.E. DeWames, D.L. Smith, J. Ehlert, , *SPIE Proceedings*, Vol. 4820, 2002
9. M.B. Reine. Ed. P. Capper and C.T. Elliot, p. 331-376. Kluwer Academic Publishers. Boston. 2001.

- 
10. D. Rosenfeld, G. Bahir, *IEEE Trans Elec Dev.*, p. 1638 –1645, Vol. 39 Num. 7, July 1992.
  11. NPOESS General Instrument Interface Document (DRAFT), August 6, 2001.
  12. J.F. Janni. TR No. AFWL-TR-65-150, September, 1966.